OPEN

The propagation characteristics of seismic waves in ultra-deep overburden by large-scale shaking table test

Yang Xing[1], Li Wentao[2✉], Wu Shibin[2], Chen Zhixiong[2] & Ding Xuanming[2]

The seismic performance of earth-rock dams on deep overburdens has long been a central focus in dam engineering. Understanding the propagation law of seismic waves within a deep overburden is key to revealing the mechanisms of the dynamic response. In this study, the propagation characteristics of horizontal and vertical seismic waves in a deep overburden were systematically investigated using large-scale shaking table tests, with analysis based on acceleration and pore pressure data combined with stockwell transforms and coherence function methods. The results show clear differences in how the deep overburden modulates seismic waves in different directions. Horizontally, seismic waves exhibit an amplitude pattern that first decreases and then increases during propagation, with low-frequency components dominating and high-frequency components being strongly filtered. Vertically, the peak acceleration at the overburden top was higher than that in the lower layers; however, the frequency content changed slightly, and high-frequency filtering was weak. The weak interlayer has an obvious filtering effect on high-frequency horizontal seismic waves. For the pore pressure response, the accumulation of excess pore pressure across different depths was generally similar; however, liquefaction was only observed at the top of the overburden.

Keywords Ultra-deep overburden, Seismic attenuation-amplification duality, Shaking table test, Propagation behavior, Bidirectional seismic wave

With the rapid development of water conservancy and hydropower projects worldwide, the problems of strong earthquakes and deep overburden foundations, which are difficult to avoid, have become important challenges for engineering construction. This is also a controlling factor for the successful construction of many projects. A deep overburden often consists of multiphase accumulations and high-variability particles interspersed with a variety of physical properties of differentiated weak interlayers[1]. Under strong earthquakes action, the dynamic response of such foundations is complex and variable, posing a major threat to engineering safety[2–4]. Therefore, for the construction of earth-rock dams built on a deep overburden, it is necessary to study the dynamic response law of the dam foundation in a deep overburden under strong earthquake action.

In recent years, seepage, seismic, and dynamic characteristics of deep overburden dam foundations have received extensive attention. Scholars have investigated seepage control wall optimization and joint stress-deformation mechanisms in core-wall dams through theoretical and numerical analyses, significantly enhancing the synergistic performance of anti-seepage systems[5–7]. Additionally, critical advancements in seismic response studies of deep overburden foundations, The nonlinear soil behavior and seismic wave propagation patterns have elucidated under dynamic loading[8–12]. Numerous scholars have systematically examined dam-foundation dynamic interactions, seepage fields, and seismic safety assessments, advancing engineering design and risk control strategies for deep overburden regions[13–16]. However, most studies have relied on idealized models and parameter simplifications. It cannot fully reflect the effects of complex multilevel layering, weak interlayers, and the physical inhomogeneity of the deep overburden on seismic wave propagation and energy evolution.

Many studies on the seismic response and dynamic hazard mechanisms of overlying dam foundations have involved shaking table tests. Zhang[17] investigated the effects of the peak input acceleration and soil layer characteristics on the propagation pattern of seismic waves using centrifuge shaking tests. The results showed that the low-frequency component was amplified and the high-frequency component was suppressed

[1]Power China Chengdu Engineering Corporation Limited, Chengdu 610072, People's Republic of China. [2]College of Civil Engineering, Chongqing University, Chongqing 400045, People's Republic of China. ✉email: hliwentao@163.com

after the seismic wave propagated through the overburden. On this basis, Peng[18] investigated the liquefaction characteristics of a 30–40 m overburden by simulating an overlying soil layer with a steel ball. Cai[19] designed a loading airbag to simulate the foundation of a sand layer at different burial depths by controlling the airbag pressure. The dynamic response and liquefaction laws of deeply buried sand foundations were studied. After the seismic wave propagates through the deep overburden, the dynamic response exhibits some attenuation, resulting in the amplification factor of the acceleration at the dam top being much smaller than the normative recommended value based on the engineering statistics of earth-rock dams over the bedrock[20]. Additionally, some studies have further realized the model size amplification and multi-field coupled monitoring by large-scale shaking table, revealing the influence of complex topography and valley effect on the seismic response of the dam body and overburden[21–25]. Despite continuous progress in shaking table test technology, we have gained a deeper understanding of the dynamic response and disaster evolution process of the dam foundation in the overburden. However, shaking table test research on complex systems of ultra-deep overburdens is still scarce.

To address the above problems, this study considers an earth-rock dam project under planning as the research object, focusing on its 500 m class ultra-deep overburden dam foundation containing weak soil layers. The spectral characteristics of the overburden were revealed through large-scale shaking table tests. Time–frequency analysis was used to study the horizontal and vertical seismic wave propagation patterns in the overburden. Furthermore, the influence of soil liquefaction and weak interlayers on the propagation of seismic waves was discussed.

Experiment setup
Engineering background
The main body of a large earth-rock dam project in western China is located on an ultra-deep overburden, which reveals that the maximum depth of the overburden is over 500 m. The regional seismic risk analysis results showed that the exceedance probability of the dam site over 100 years was 2% and the peak horizontal acceleration of the bedrock exceeds 0.5 g. Combined with the drilling survey data of the dam site, the foundation of the entire overburden was mainly composed of six soil layers. Layer ① is mainly composed of yellow gravel soil and sand-containing gravel soil, and the maximum thickness can reach 180 m. Layer ② was mainly composed of gray gravel with a maximum thickness of 150 m. Layer ③ is composed of medium coarse and medium fine sand containing gray gravel, with a maximum thickness of 150 m. Layer ④ was a silty clay layer (commonly termed "weak interlayers" in engineering practice) with a maximum thickness of 20 m. Layer ⑤ is mainly composed of coarse sand and fine sand with gray gravel, with a maximum thickness of 60 m. Layer ⑥ is mainly composed of gray-yellow sand gravel layers, with a maximum thickness of 20 m.

Numerous site investigations were conducted during the engineering design and planning stages. Field soil samples were taken to the laboratory for triaxial dynamic characteristic tests. These field investigations and laboratory tests can be used as the basis for subsequent research[12,26,27]. The physical and mechanical parameters of the soil samples are listed in Table 1.

Shaking table and model box
In this study, a large three-dimensional six-degree-of-freedom shaking table from the Shaking Table Laboratory of Chongqing University was used. The table size is 6.1 × 6.1 m, the maximum load capacity is 60 tons, the two horizontal maximum acceleration is 1.5 g, the vertical maximum acceleration is 1.0 g, and the system operating frequency is 0.1-50 Hz.

A steel layered shear box with a length of 1.5 m, a width of 1.5 m, and a height of 3.5 m is designed, as shown in Fig. 1. The shear box provided flexible constraint boundary conditions for the rock and soil mass by superimposing 35 layers of rectangular shear rings. The model box and shaking table were fixed with high-strength bolts to improve the movement consistency between the model box and shaking table so that the movement of the table surface could be better transferred to the soil layer model. A layer of 2 mm rubber mold was laid on the surface of the shear box to ensure the tightness of the model box and prevent soil particles from entering the shear ring. A layer of geotextile was laid on the inner and outer surfaces of the rubber mold to prevent uneven parts of the model box and soil particles from puncturing.

Similarity ratio design
To simulate the seismic response of an ultra-deep overburden, similarity requirements must be considered. Scholars have conducted detailed research on the similarity theory of model tests[28,29]. In this study, the seismic

Soil Layers	Soil layers	Saturated density (g/cm³)	Void ratio e	Dry density (g/cm³)	Shear strength Φ (°)	C (kPa)	Permeability coefficient (cm/s)
⑥	sand gravel	2	0.65	1.61	35	0	1.5×10^{-2}
⑤	coarse sand	1.95	0.57	1.58	27	0	2.5×10^{-3}
④	silty clay	1.98	0.82	1.53	22	13	3.1×10^{-6}
③	medium fine sand	2	0.55	1.65	28	0	1.4×10^{-3}
②	sand gravel	1.98	–	–	37	0	5×10^{-3}
①	sand gravel	1.97	–	–	39	0	1×10^{-4}

Table 1. Dimensions of each soil layer in the shaking table test model.
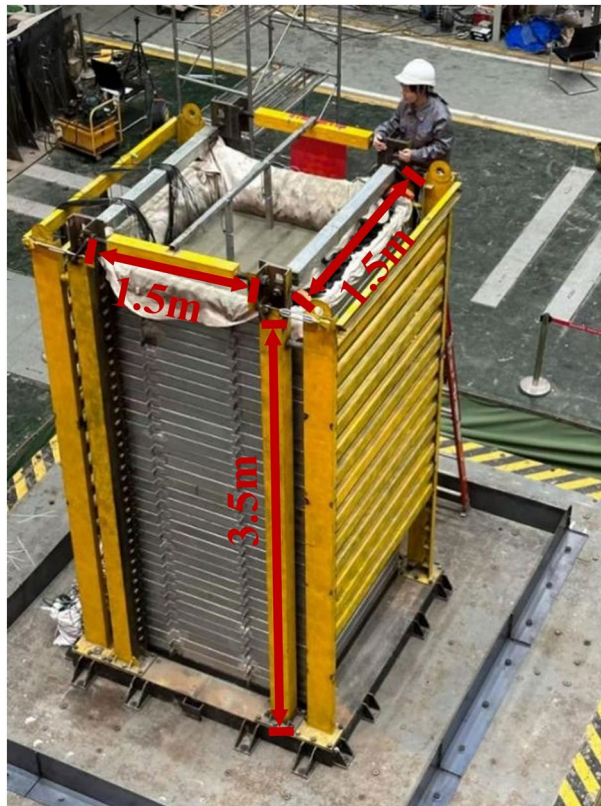
Fig. 1. Shaking table and laminar box.

Physical quantities	Parameters	Similarity relationship	Similarity coefficient
L	Size	C_l	180
ρ	Density	C_ρ	1
g	Acceleration	C_g	1
σ	Stress	$C_\sigma = C_l$	180
ε	Strain	C_ε	1
E	Modulus of elasticity	$C_E = C_l$	180
μ	Displacement	$C_\mu = C_l$	180
t	Time	$C_t = C_l^{1/2}$	13.42
ν	Frequency	$C_\nu = C_l^{-1/2}$	0.075

Table 2. Similarity constants of shaking table test.

acceleration, density, and geometric size were selected as control parameters, and the test geometric size similarity ratio was set to 180, based on the size of the model box and the actual parameters of the ultra-deep overburden. The parameters of the other physical quantities are listed in Table 2, and the thickness of each soil layer is listed in Table 3.

Model preparation

The material used in the model soil mass was collected from a dam construction site. According to the size of the model box, particles greater than 60 mm in the soil mass will have a non-negligible size effect; therefore, the removal method was adopted to remove particles greater than 60 mm. Because layers ① and ② are hundreds of meters underground, it is not easy to obtain raw materials on-site; therefore, layer ⑥ of soil material was used instead. In this test, layer ④ mainly plays the role of a non-liquefied waterproof layer; therefore, there is no need to consider the parameters of layer ④, and a certain amount of water can be weighed to obtain a soft plastic shape. Figure 2 shows the particle gradation of each soil layer during testing.

The construction process of the model is shown in Fig. 3. First, the geotextile and rubber mold were laid inside the model box and the flower tubes were embedded. The model was prepared by controlling the dry density. The model was filled in layers, with a total of 32 layers, each layer 10 cm. The soil sample should be fully

Soil layer number	Model size (m)	Prototype size (m)
⑥	0.11	20
⑤	0.33	60
④	0.11	20
③	0.83	150
②	0.83	150
①	1.0	180
Total	3.22	580

Table 3. Dimensions of each soil layer in the shaking table test.
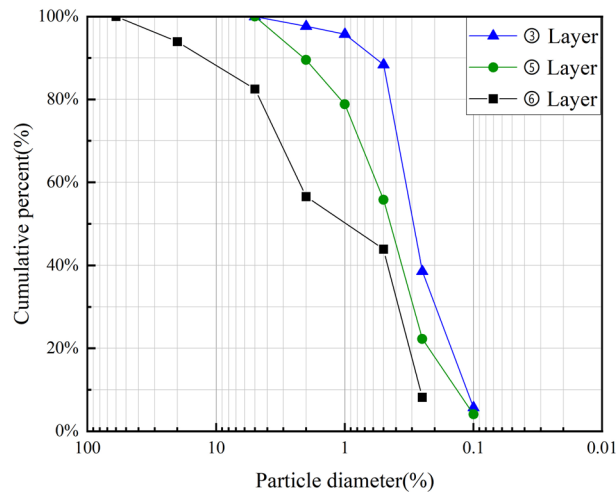
Fig. 2. Particle size distribution curves of the model materials.

rammed and the compacted soil layer should be sampled and tested to ensure that the designed dry density can reach[14]. After the filling reached the design height, water was added to the saturated soil material until the water level was 1 cm higher than the surface and the soil was allowed to stand for 24 h. If the water level decreased, water was added to ensure that the soil sample was fully saturated. Because of the water-insulating effect of layers ④ of clay, buried water pipes were connected to the upper and lower layers in advance to discharge the gas, add water saturation, and block the water pipes after saturation to prevent the formation of water channels above and below layer ④ and affect the test results.

The sensor layout is shown in Fig. 4, a total of 30 acceleration sensors are installed in the soil mass. The acceleration sensors were unidirectional and mainly measured the acceleration response in the X- and Z-directions, including 20 pore pressure sensors, 18 earth pressure sensors, and two displacement sensors. To minimize the effects from the shear box boundary conditions, the sensors were buried at least 50 cm from the boundary.

### Input motion and test arrangement
In this study, the acceleration time-history curve was used to simulate the seismic waves. Artificial seismic waves are used in this study. Its acceleration time-history curve comes from the study of similar engineering projects by related researchers, and its amplitude magnitude takes full account of the seismic hazard of the dam site[12,30]. Taking 0.1 g artificial seismic wave as an example, the acceleration time-history curve and Fourier spectrum are shown in Fig. 5 and Fig. 6. The main frequencies of the horizontal acceleration was 1.50 Hz, and that of the vertical acceleration were 2.04 Hz. In the test, two directions were simultaneously loaded (X- and Z-directions), and the peak value of the acceleration in the Z-direction was taken as 2/3 of that in the X-direction. The test conditions are listed in Table 4. White noise was inputted before loading to obtain the natural vibration characteristics of the system. Part of the prototype artificial waves was applied at the end of the test to study the dynamic response of seismic waves to an ultra-deep overburden.

Result and analysis
Dynamic characteristics of ultra-deep overburden
White noise was input before loading to obtain the natural vibration characteristics of the entire system of the model box and soil mass. The A1-A9 acceleration sensor were selected for this study. Figure 7 shows the FFT spectra of the horizontal and vertical monitoring points under the action of white noise. "%H" is the percent height of the overburden; the "MF" is the main frequency of the acceleration. As shown in Fig. 7, the horizontal
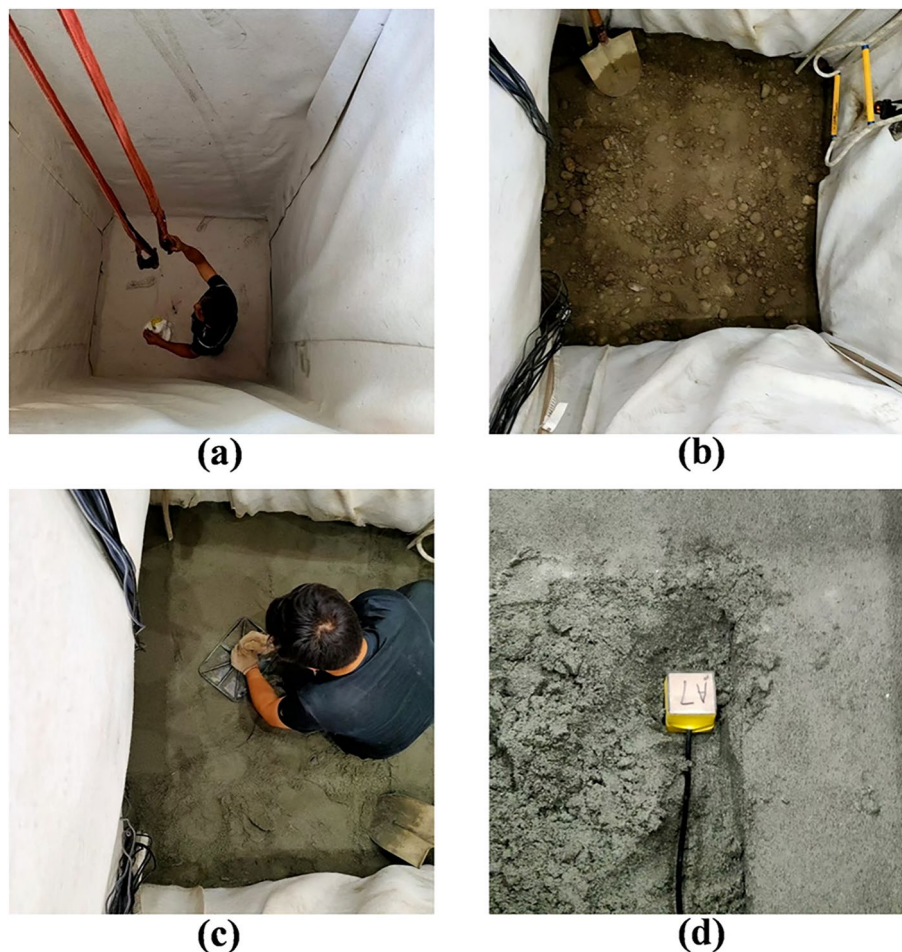
Fig. 3. Model construction process: (**a**) laying geotextile, (**b**) filling earth, (**c**) rammed earth, and (**d**) embedded sensors.

natural vibration frequency mainly ranges from to 2–20 Hz, and the bottom of the soil layer was 20.66 Hz. At the top, the frequency decreases to 1.97 Hz. The vertical natural vibration frequency was mainly concentrated in the range 9–16 Hz, and that at the bottom was 15.68 Hz. With an increase in height, it decreases to 9.01 Hz and remained unchanged. In addition, the low frequency was amplified, and the high frequency was suppressed in both the vibration directions. Owing to the laminar box model, the soil mass can shear in the horizontal vibration direction, whereas the vertical vibration is fixed at the bottom, resulting in a horizontal natural vibration frequency that is lower than the vertical vibration.

The Quarter-Wavelength Method[31] (QWL, $f = Vs/4H$) was used to calculate the main frequency of the soil layer, and the theoretical value was compared and analyzed with the measured main frequency of the acceleration response in the test. QWL is one of the most widely used simplified methods for the analysis of the horizontal seismic wave dynamic response of layered soils, and its principle is based on the propagation characteristics of shear waves in soils. The site response under seismic action is dominated by horizontal shear waves, and the dynamic response and damage modes of most engineering structures are related to horizontal seismic waves. The theoretical main frequency calculations and experimental comparisons were centered on the horizontal component, and the main frequency of the vertical component was not included in the scope of the comparisons in this study. The shear wave velocity in the theoretical calculation was derived from the survey data of the actual site[12], and the thickness was calculated based on the prototype obtained from the test similarity ratio. The longitudinal distribution patterns of the theoretical and measured main frequencies of the tests for different soil layers are shown in Fig. 8. In general, the theoretical main frequency increased rapidly with the height of the soil layer, reflecting the frequency distribution characteristics of higher-order modes under ideal conditions. Although the measured main frequency was much lower than the theoretical value overall, except for the bottom two layers of the overburden. The main reasons for this difference may be the damping of the actual soil layer, energy dissipation of the weak interlayer, and the limited response sensitivity of the test system in the high-frequency band.
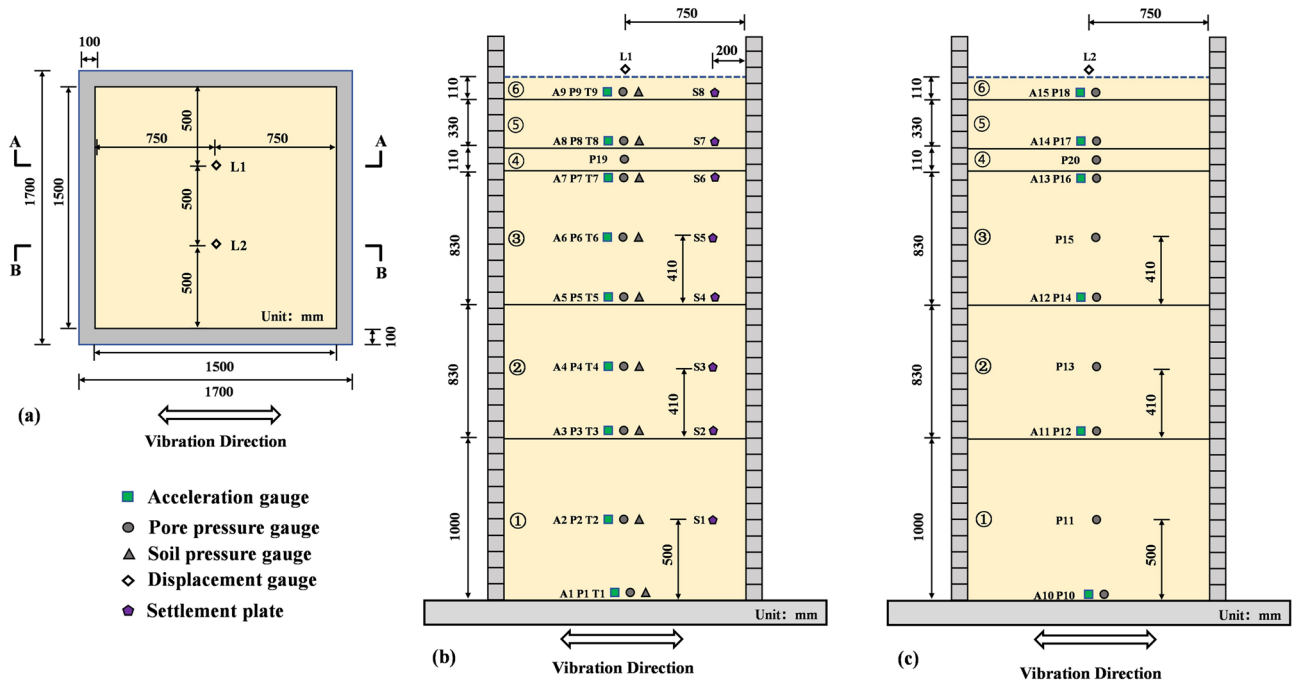
Fig. 4. Schematic diagrams of the model test: (**a**) plane view, (**b**) sectional view (A–A), and (**c**) sectional view (B–B). Note: Acceleration and soil pressure gauges measured the horizontal and vertical directions, respectively.
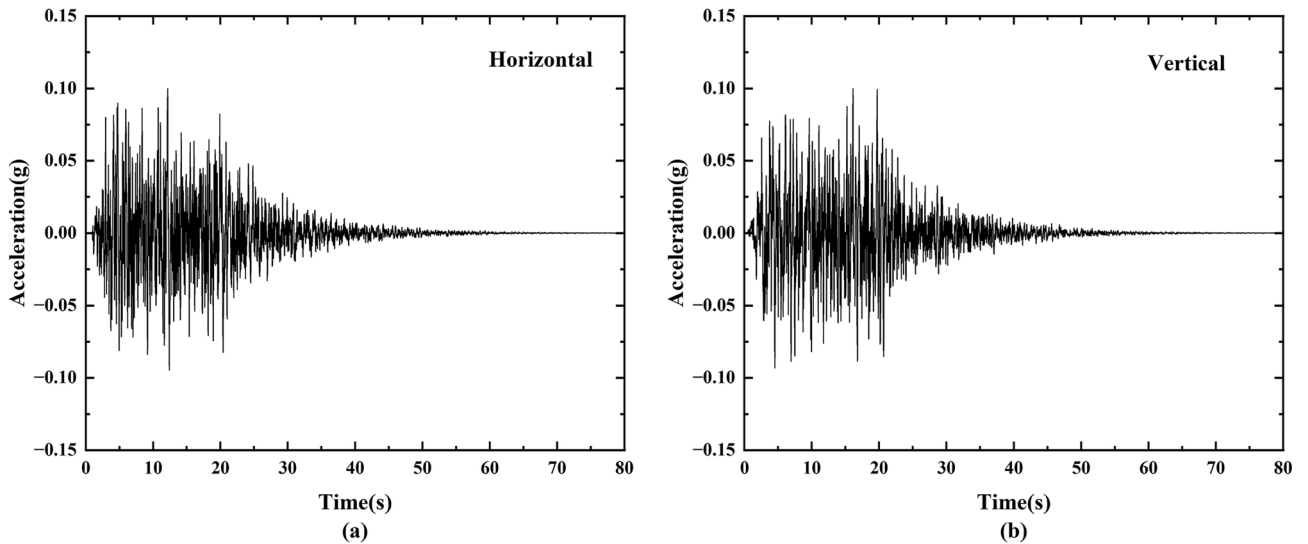
Fig. 5. Selected input motions used during the tests: (**a**) horizontal and (**b**) vertical.

Acceleration

Figures 9 and 10 show the distribution of the acceleration amplification coefficient and normalized main frequency factor along the overburden heights of the overburden under different peak ground accelerations (PGA). Both the acceleration amplification coefficient and normalized main frequency factor at the bottom of the model were 1. With increasing height, the horizontal acceleration amplification coefficient gradually decreased, whereas the vertical acceleration amplification coefficient gradually increased, and the normalized main frequency factor of acceleration in both directions decreased. With an increase in the input PGA, the horizontal acceleration amplification factor decreased and stabilized when the PGA was 0.48 g. However, the vertical acceleration amplification factors were different and there was no obvious regularity. The distributions of the normalized main frequency factor of the acceleration in the two directions were different. The horizontal normalized main frequency factor of each magnitude was significantly different in layers ② and ③, whereas
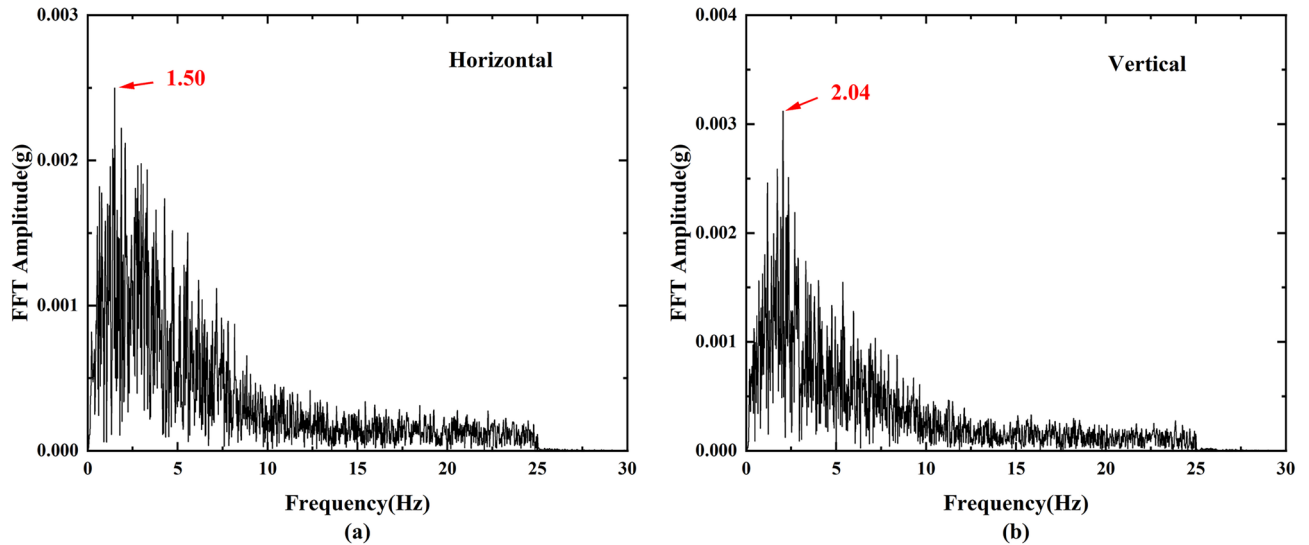
Fig. 6. Fourier spectra of input motions: (**a**) horizontal and (**b**) vertical.

Test no.	Input motions	Intensity (g)		Remark
		X	Z	
Case1	WN-1	0.05	0.05	White noise
Case2	AS-1	0.1	0.07	
Case3	AS-2	0.24	0.16	
Case4	WN-2	0.05	0.05	White noise
Case5	AS-3	0.48	0.32	
Case6	WN-3	0.05	0.05	White noise
Case7	AS-4	0.62	0.41	
Case8	WN-4	0.05	0.05	White noise
Case9	AS-5	0.8	0.53	
Case10	WN-5	0.05	0.05	White noise
Case11	AS-6	0.1	0.07	Prototype wave
Case12	AS-7	0.24	0.16	Prototype wave
Case13	WN-6	0.05	0.05	White noise
Case14	AS-8	0.48	0.32	Prototype wave
Case15	WN-7	0.05	0.05	White noise

Table 4. Test arrangement. WN represents white noise; AS represents the artificial wave.

the vertical normalized main frequency factor remained unchanged at 0.07 g and the other magnitudes first increased and then decreased.

Figure 11 shows the variation in the acceleration amplification coefficients and normalized main frequency factors at the top of the overburden. Horizontally, the maximum acceleration amplification coefficient is 1.17, which occurs at a PGA of 0.8 g, while the maximum vertical acceleration amplification coefficient is 2.7, which occurs at a PGA of 0.53 g. With the increase in PGA, the horizontal acceleration amplification coefficient first decreases and then tends to be stable, and its normalized main frequency factor changes little, with the maximum being 0.17 and the minimum being 0.14. Vertically, with an increase in the PGA, the amplification coefficient first decreased and then increased, whereas the normalized main frequency factor decreased gradually, with a maximum of 0.6 at 0.07 g and a minimum is 0.34 at 0.53 g.

Figures 12 and 13 show the acceleration time-history curve and the corresponding main frequency at horizontal PGA of 0.48 g and vertical PGA of 0.32 g. The results show that the horizontal peak acceleration decreases to 0.22 g at the top (A9), a decrease of 54.17%, with an increase in height. In the vertical direction, the peak acceleration increases to 0.69 g, an increase of 115.63%. The main frequencies corresponding to both directions decrease with increasing height. The main frequency of horizontal seismic wave propagating from the bottom to the top decreases from 15.54 to 2.23 Hz, and the main frequency in the vertical direction decreases from 21.07 to 8.94 Hz.
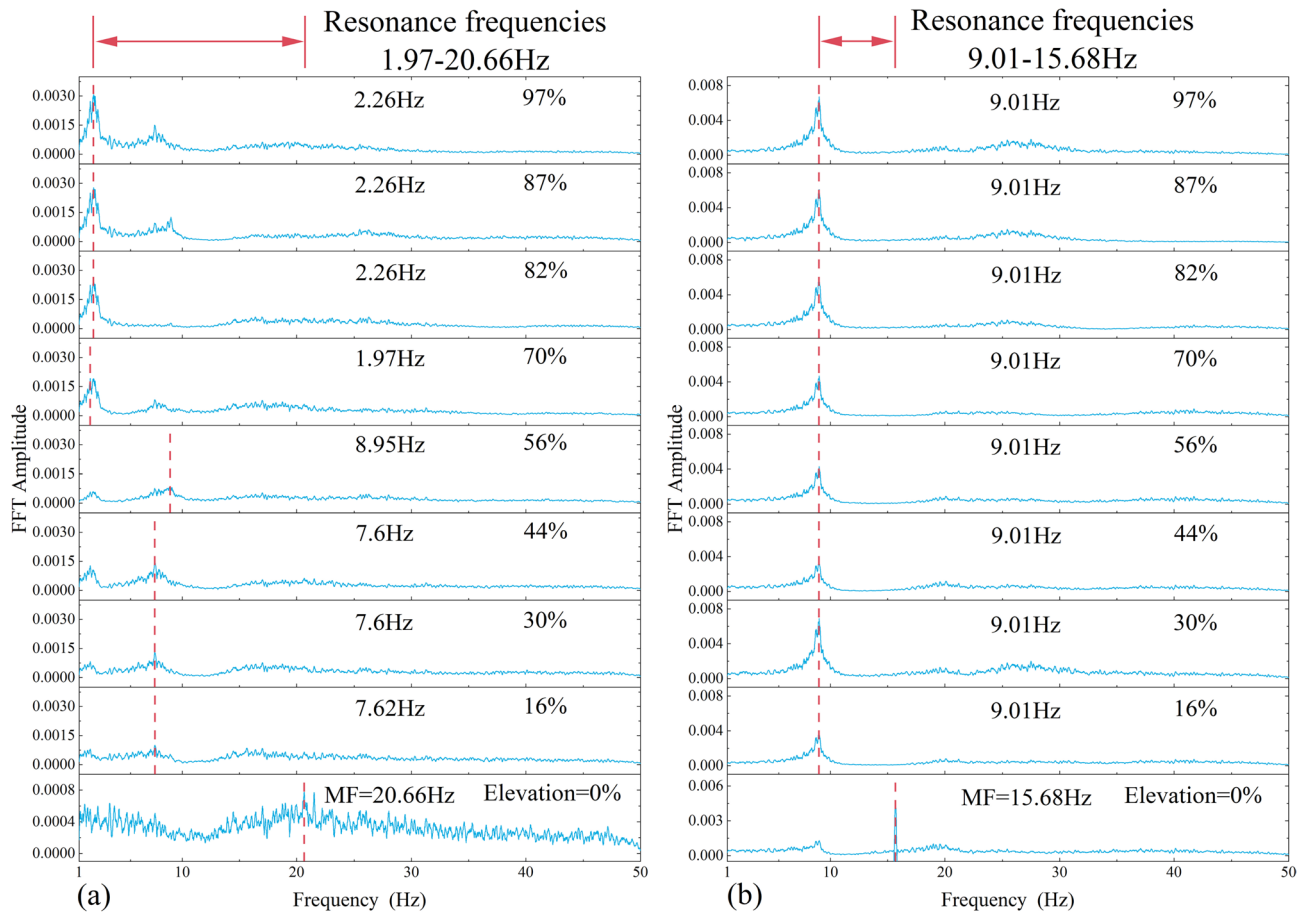
Fig. 7. Spectrum characteristics of the overburden: (**a**) horizontal and (**b**) vertical.
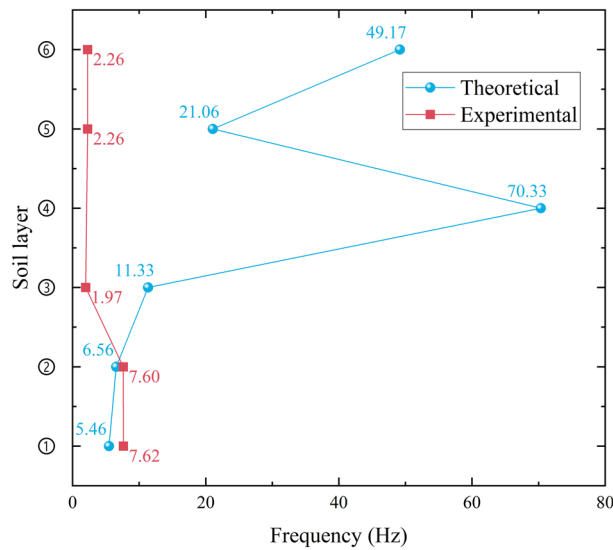
Fig. 8. Variation of main frequency with overburden height.
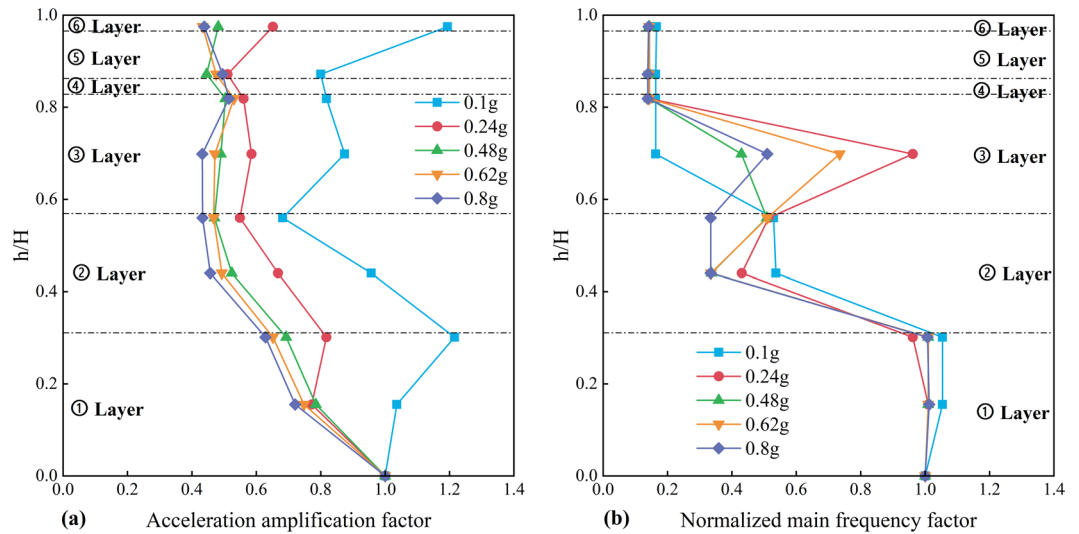
Fig. 9. Distributions of the horizontal acceleration amplification factor and normalized main frequency factor along the height of the overburden: (**a**) distributions of the acceleration amplification factor and (**b**) normalized main frequency factor.
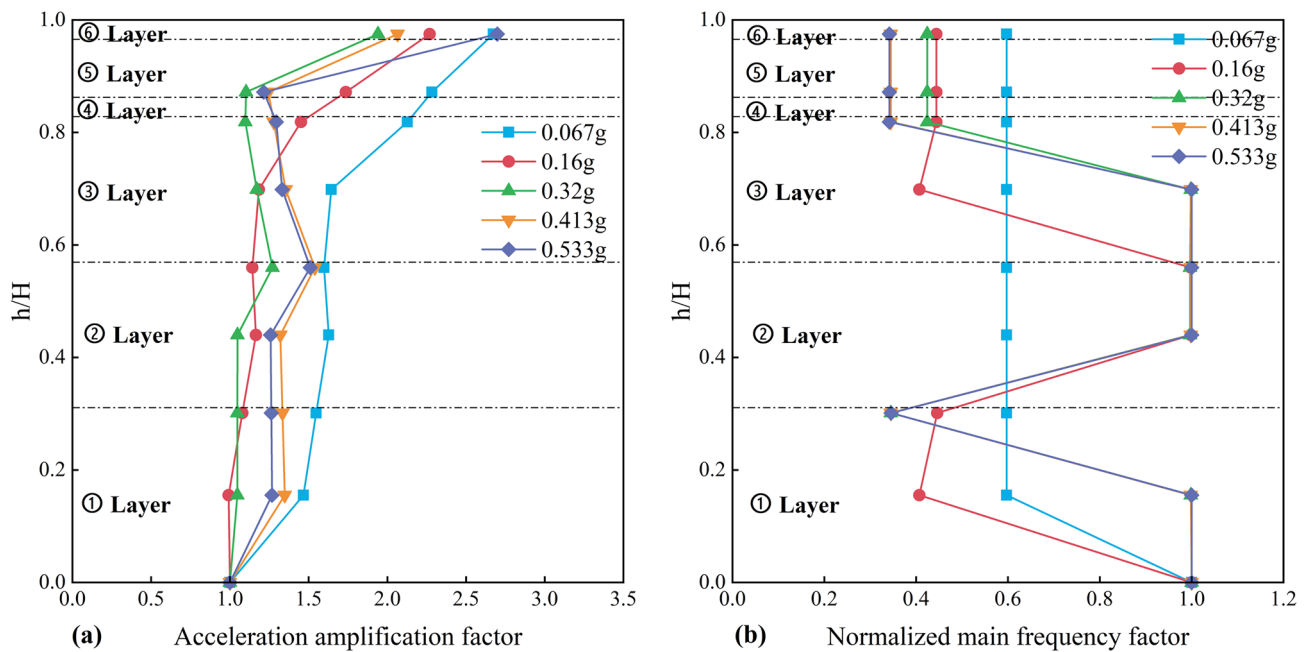
Fig. 10. Distributions of vertical acceleration amplification factor and normalized main frequency factor along the height of the overburden: (**a**) distributions of acceleration amplification factor and (**b**) normalized main frequency factor.

Owing to the soil container, the soil mass can be sheared in the horizontal vibration direction, while the vertical bottom is fixed. When seismic waves are applied, the soil particles in the horizontal direction are more likely to slide with each other, and the fundamental frequency of the overlying layer decreases. This causes the natural frequency of the overlying layer to deviate from the main frequency of seismic motion, resulting in a decrease in the horizontal acceleration amplification factor. The shear effect was more evident and the magnification coefficient was further reduced. However, owing to the constraints in the vertical direction, the stiffness decreased less, the fundamental frequency of the overburden layer gradually decreased, and it was close to the main frequency of the input seismic wave. Therefore, the overburden layer was more likely to resonate with the input seismic acceleration, and the amplification coefficient of the vertical acceleration increased.

To further investigate the propagation patterns of the seismic waves. A time–frequency analysis (Stockwell transforms) of the acceleration data was performed[32,33]. Figure 14 shows the propagation pattern of the
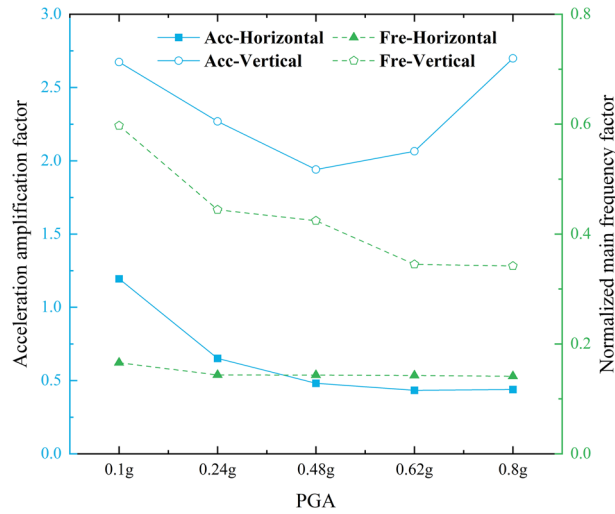
Fig. 11. Acceleration amplification factor and normalized main frequency factor of top of overburden.
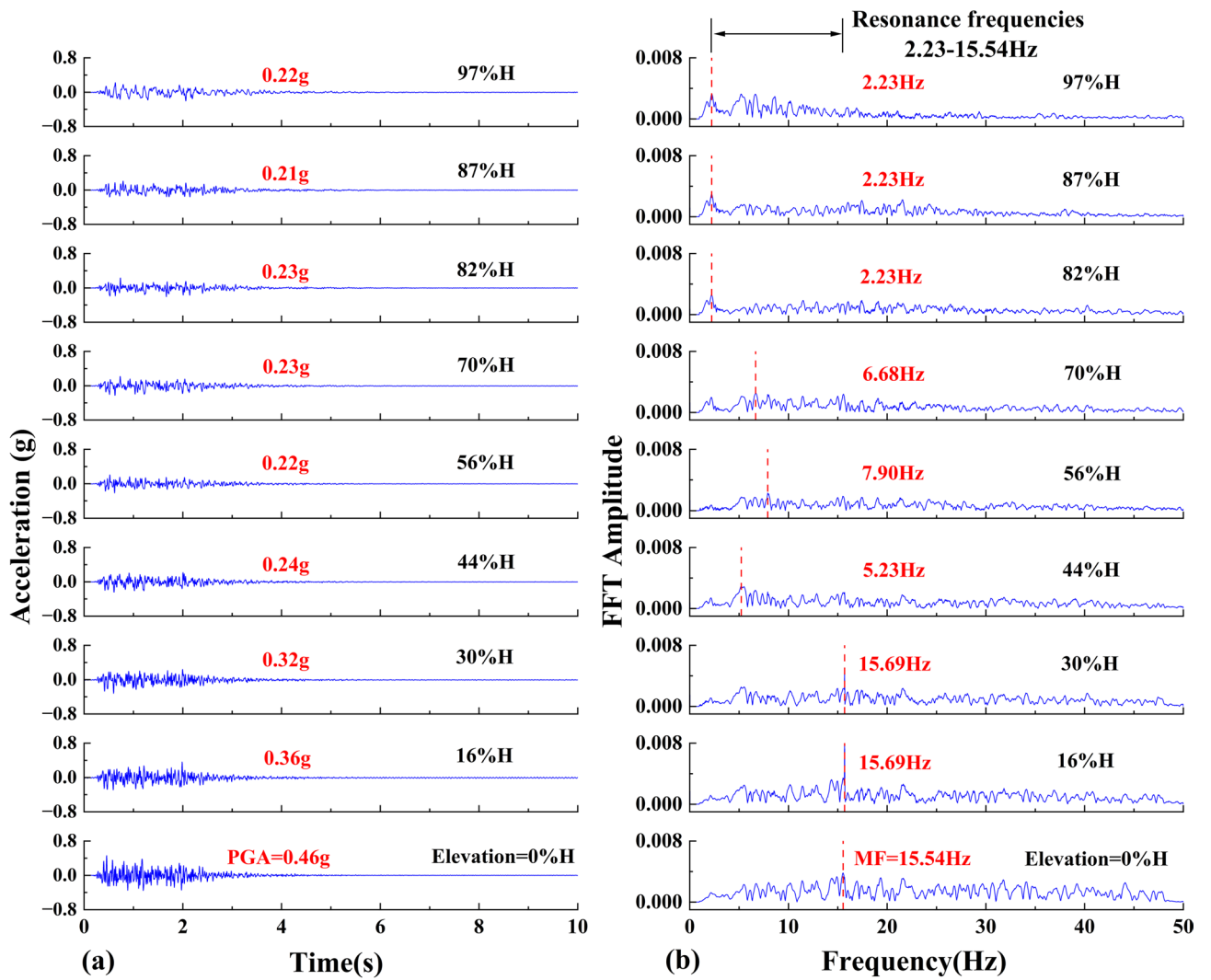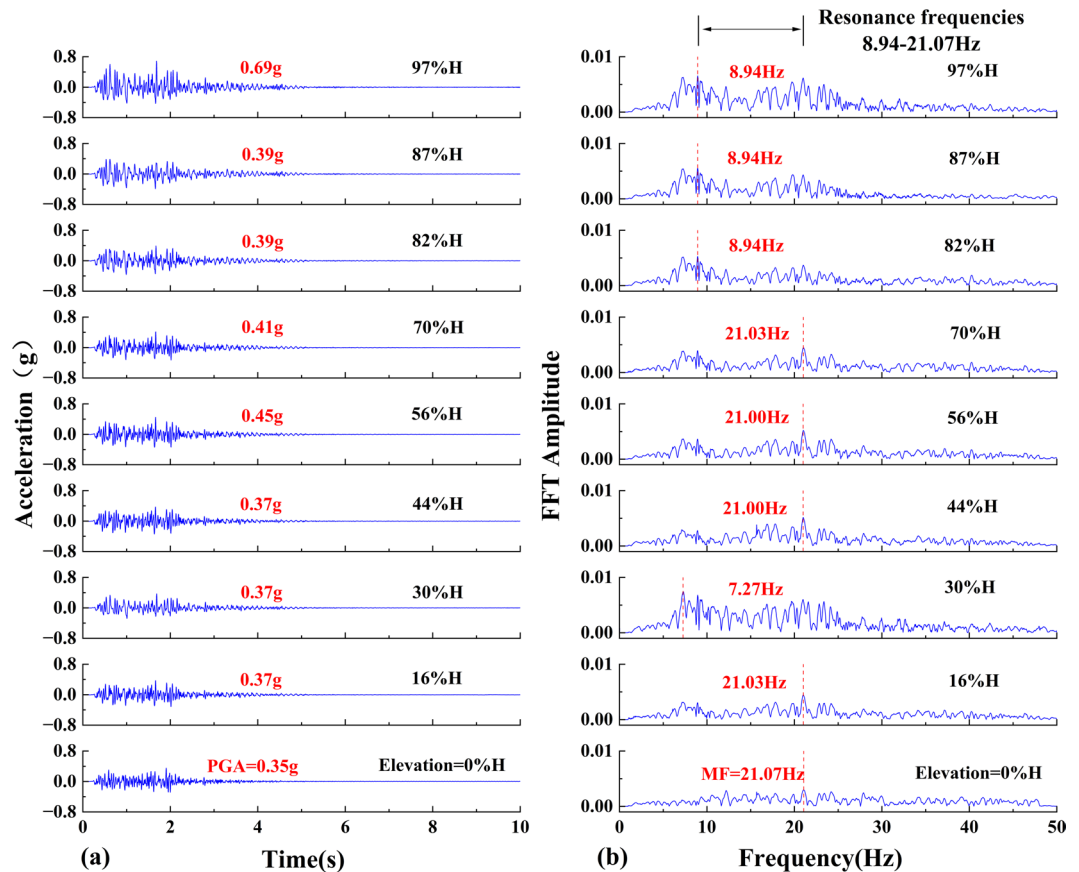

Fig. 12. Records of the horizontal acceleration-time history and Fourier spectra at different heights (Case 5): (**a**) acceleration-time history and (**b**) Fourier spectra.

Fig. 13. Records of vertical acceleration-time history and Fourier spectra at different heights (Case 5): (**a**) acceleration-time history and (**b**) Fourier spectra.

seismic waves along the overburden at a PGA of 0.48 g. The effective action time of the seismic wave is mainly concentrated between 0 and 2.5 s. The peak acceleration continued to decrease as the horizontal seismic wave propagated upward, and energy was transferred from the high-frequency band to the low-frequency band. At the bottom of the overburden, the energy was primarily concentrated at 15–47 Hz, whereas at the top it was concentrated at 4–11 Hz. The energy of the vertical seismic wave was mainly concentrated at 13–34 Hz, After passing through different soil layers, the change was small, but the peak acceleration increased. This indicates that the overburden has a difference in the modulation mechanism of the seismic waves in different directions. Combined with Fig. 7, the resonance bands of the seismic waves in different directions are different, which may be an important reason for this modulation difference.

Pore pressure

Figure 15 shows the variation in the excess pore pressure ratio with overburden height. The excess pore pressure ratio gradually increases as the input PGA increases. However, in the middle and lower parts of the overburden, the excess pore pressure ratio was small. The excess pore pressure ratio showed an abrupt decrease in the weak interlayer until the top of the overburden, where the increase was significant. At a PGA of 0.48g, the excess pore pressure ratio exceeded 1 for the first time, which indicated that liquefaction started to occur at the top of the overburden. However, at a PGA of 0.62 g, the excess pore pressure ratio decreased. This may be a result of repeated liquefaction, which causes rearrangement of soil particles and increases the relative compactness of the soil[34]. The test results showed that liquefaction occurred only at the top of the overburden, regardless of the input PGA, which is probably because the effective stress at the top of the overburden is small and liquefaction occurs easily.

To further investigate the link between acceleration and pore pressure, the effect of liquefaction on acceleration was investigated. Combined analysis of acceleration and pore pressure of the overburden[35,36]. Figure 16 shows the acceleration (Stockwell transforms) and excess pore pressure variations in the overburden. The variations in the excess pore pressure were similar at all locations in the overburden. When the PGA is 0.24 g, the overburden has a dynamic response, but the excess pore pressure has not accumulated to the critical value of liquefaction, and the S-transform spectrum energy is concentrated and the amplitude is small. With the increase of PGA to 0.48 g, the top of the overburden firstly reaches liquefaction, and the accumulation of excess pore pressure
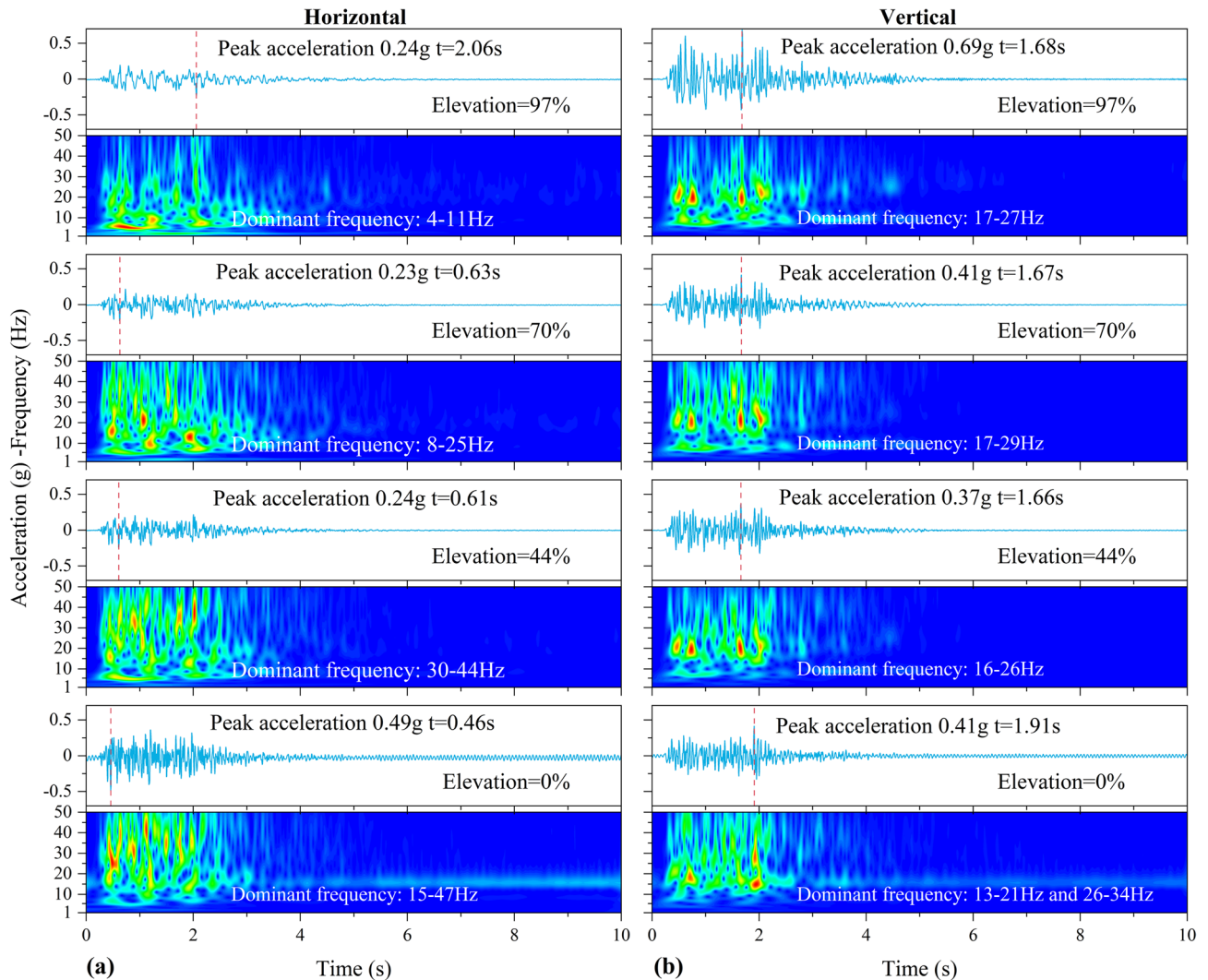
**Fig. 14**. Time-history and stockwell transformation of accelerations: (**a**) horizontal, (**b**) vertical.

is obvious, accompanied by the enhancement of low-frequency energy, which reflects the strong nonlinear dynamic process of the soil body and the behavior of local liquefaction dissipation.

In this test, at a lower input PGA, the acceleration at the top of the overburden exhibits amplification owing to the integrity and stiffness of the soil, which effectively transmits and amplifies seismic wave energy. As the input PGA increased and approached a critical threshold, the excess pore pressure gradually increased and the effective stress decreased towards zero. When the top of the overburden starts to liquefy, its strength and stiffness decrease sharply, resulting in a significant reduction in acceleration amplification (the amplification factor decreases), and even attenuation can occur. This transition from amplification to attenuation was mainly controlled by the pore pressure buildup and the onset of liquefaction.

Influence of weak interlayer on seismic wave propagation

Weak interlayers have a significant impact on the propagation of seismic waves, and previous studies have shown that weak interlayers can absorb or amplify seismic waves[37]. In this study, the acceleration amplification factor of the weak interlayer was defined as the ratio of the peak acceleration of the monitoring point (A8) above the weak interlayer and the measurement point (A7) below the weak interlayer. Figure 17 shows the distribution of the acceleration amplification coefficient of the weak interlayer. With an increase in the acceleration, the horizontal amplification coefficient was always less than 1, and the minimum was 0.88. In contrast, the vertical amplification coefficient first increases and then decreases.

Figure 18 shows that the acceleration stockwell transforms the results of the upper and lower measurement points of the weak interlayer, which contain horizontal and vertical seismic wave components, respectively. As can be seen in Fig. 18, the horizontal seismic wave shows a strong energy response in the 10–30 Hz band. However, the high-frequency energy zone shrinks rapidly and attenuates after crossing a weak interlayer. This indicates that the weak interlayer has a strong damping effect on high-frequency horizontal seismic waves. In contrast, the vertical seismic wave component energy was mainly concentrated in the lower frequency band (10–20 Hz),
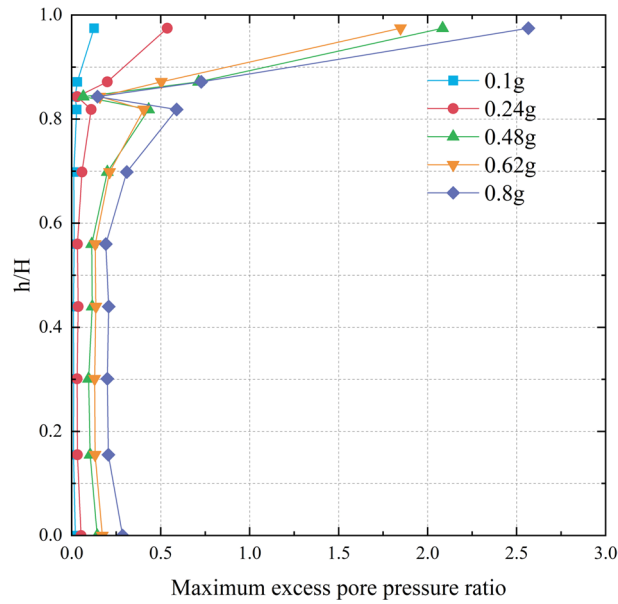
**Fig. 15**. Variation of excess pore pressure ratio along the height of the overburden.
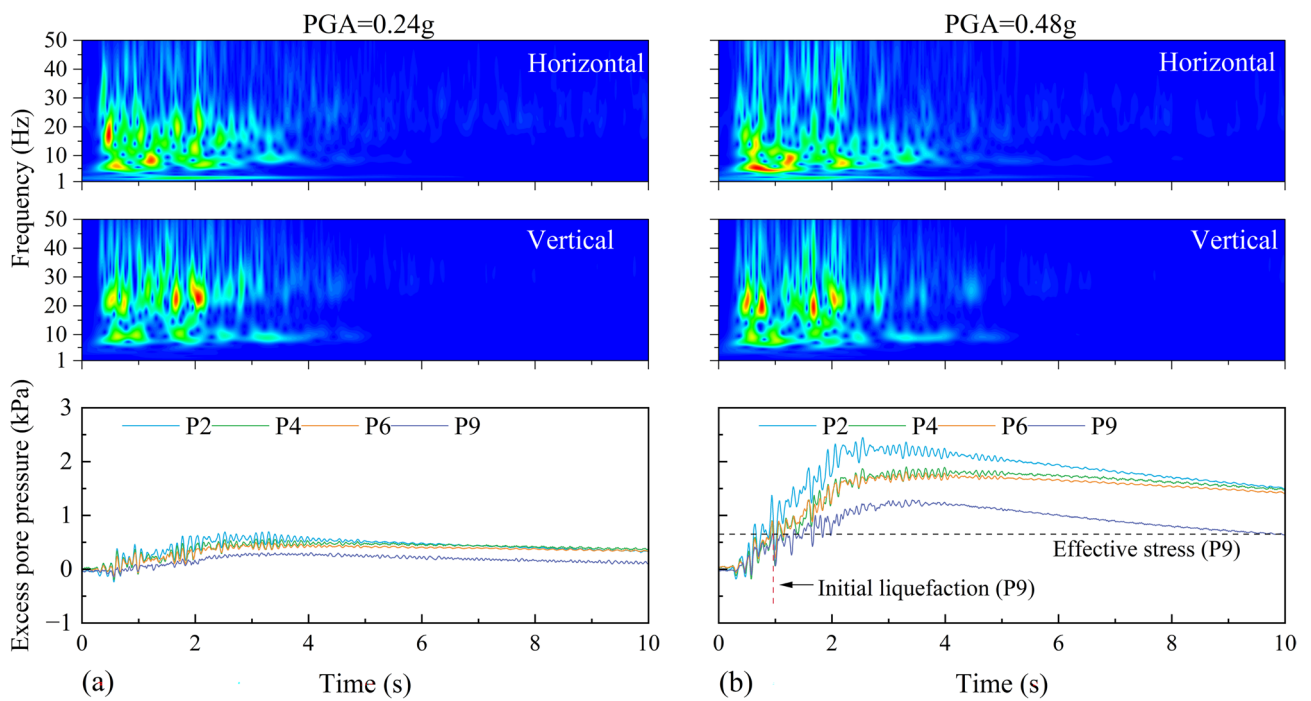
Fig. 16. Time-history variation of acceleration and pore pressure at the top of the overburden at a PGA of 0.48 g.

and the difference in the time–frequency energy distribution between the upper and lower measurement points of the sandwich was relatively small. This indicates that the weak interlayer had a stronger filtering effect on the horizontal high-frequency seismic energy and a limited effect on the vertical energy. The test results revealed the frequency-selective energy-dissipation mechanism of the weak interlayer, which is of great significance for guiding the seismic wave response of the site and the design of the engineering foundation.

Coherence is an indicator in the frequency domain that measures the degree of linear correlation between two signals in specific frequency components, with a value range of [0, 1]. The value is 1: and the two signals are linearly correlated at this frequency. Value 0: There is no linear correlation between the two signals at this frequency. The specific calculation formula for coherence is as follows
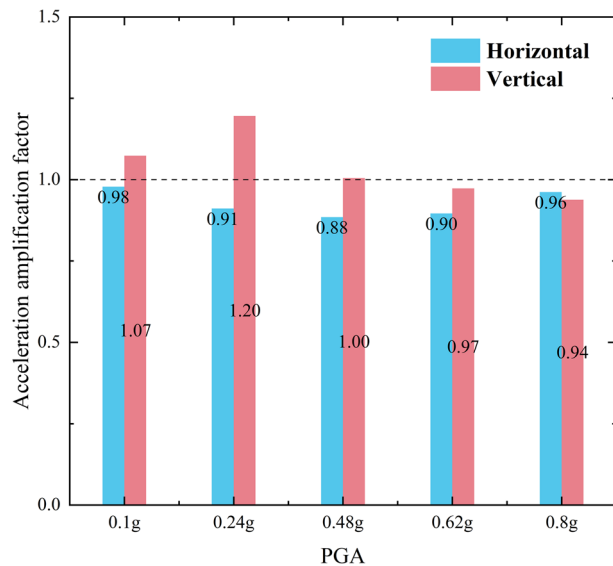
Fig. 17. Acceleration amplification factor of the weak interlayer.
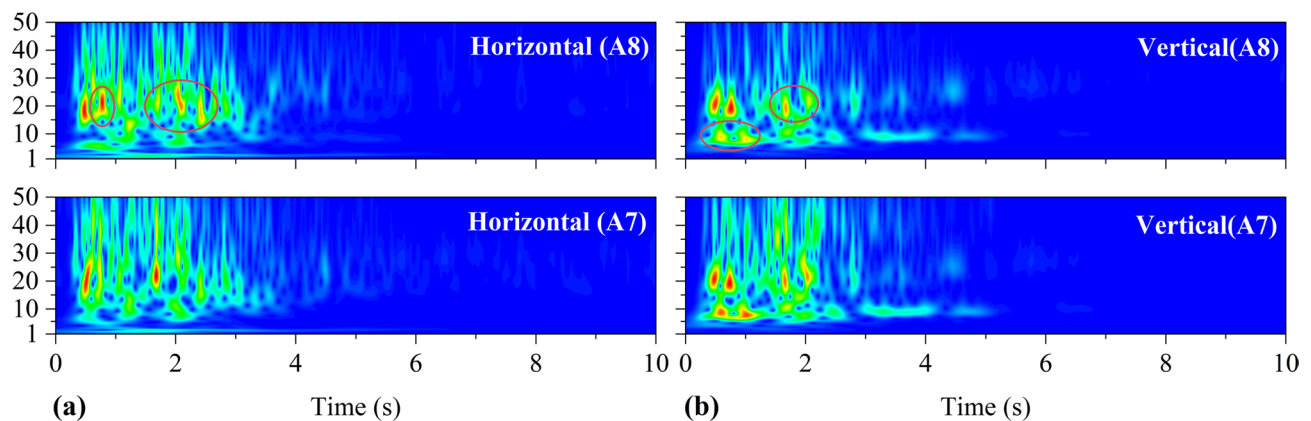
Fig. 18. Time-history variation of acceleration at a PGA of 0.48 g.

$$\gamma^2(f) = \frac{|S_{xy}(f)|^2}{S_{xx}(f)S_{yy}(f)} \tag{1}$$

$S_{xy}(f)$: Cross-power spectral density (CPSD) of signals $x(t)$ and $y(t)$.

$S_{xx}(f)S_{yy}(f)$: Auto-power spectral density (APSD) of $x(t)$ and $y(t)$.

Figure 19 shows the acceleration coherence results of the measurement points above and below the weak interlayer. The coherence of the acceleration signals above and below the weak interlayer in the horizontal direction is much lower than that in the vertical direction, particularly in frequency bands of 10–40 Hz. Some of these are reduced to 0.4–0.6, which indicates that the weak interlayer has a more evident frequency-dependent energy dissipation effect on the horizontal transmission of the seismic wave, and the low-coherence intervals correspond to significant damping. The coherence was close to 1 at most frequencies in the vertical direction, indicating that the effect of the weak interlayer on the energy transmission of the vertical seismic wave was small, and the fluctuation was mainly linear with limited energy loss. This may be related to the tectonic anisotropy of the interlayer or to a sudden change in the transverse wave impedance of the material.

Conclusions

Through a large-scale shaking table model test, the seismic wave propagation law of a dam foundation under a strong earthquake (peak acceleration exceeding 0.5 g) with a 500 m class ultra-deep overburden was studied. The following conclusions were drawn.

(1) The seismic wave propagation patterns in the overburden differed by direction. Horizontally oriented seismic waves first decrease and then increase in amplitude with height, whereas vertically oriented waves are
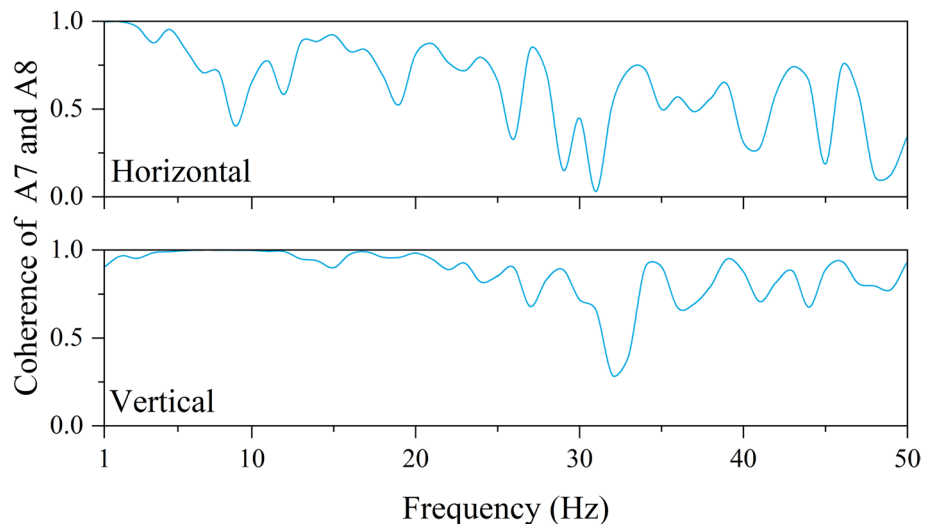
Fig. 19. Coherence of acceleration at a PGA of 0.48 g.

primarily amplified, particularly at the top of the overburden. In both directions, the dominant frequency generally decreases with increasing height.

(2) Liquefaction occurs only at the top of the overburden regardless of the input PGA. When liquefaction occurs, acceleration is attenuated, high-frequency components of horizontal seismic waves are filtered out, and the frequencies of the vertical seismic waves change slightly.

(3) Weak interlayers also exhibit direction-dependent modulation. Horizontal seismic waves passing through a weak interlayer exhibit poor coherence and significant energy dissipation in the high-frequency range; however, their effect on the energy transmission of vertical seismic waves is minimal.

This study had several limitations. First, the shaking table model is subject to scaling laws and boundary effect constraints, which may influence the dynamic responses compared to full-scale field conditions. Second, the soil profile was simplified and may not capture the full complexity of the natural site stratigraphy or in situ properties. Third, the use of artificially synthesized earthquake inputs, while representative, does not encompass the full spectrum of natural ground motion variability. In the follow-up work, we will consider conducting larger modeling tests in order to minimize the influence of the boundary and also to construct the structure of the ultra-deep cover closer to the natural state. For the input ground motions, several types of natural seismic waves will be selected for subsequent tests in order to better study the propagation characteristics of seismic waves in the ultra-deep overburden.

Data availability

References

1. Yan, Z. et al. Distribution characteristics and geogenic mechanisms of riverbed overburden in Southwest China. *Front. Earth Sci.* **10**, 895769 (2022).
2. Hedayati, H. et al. Assessment and presentation of a treatment method to seepage problems of the alluvial foundation of ghordanloo dam. *NE Iran. J. Geol. Soc. India* **85**, 377–384 (2015).
3. Luo, Y. et al. Effect of open-framework gravel on suffusion in sandy gravel alluvium. *Acta Geotech.* **15**, 2649–2664 (2020).
4. Zhang, X. et al. Geological implication of the Jinsha River flowing eastward,ancient dammed lake deposition,and quaternary river evolution in China. *Mt. Res.* **38**, 805–815 (2020).
5. Zou, D. et al. Refined analysis on stress state of cutoff wall of high asphaltic core dam on super-deep overburden. *Rock Soil Mech.* **44**, 1826–1836 (2023).
6. Zou, D. et al. Deformation mechanism and optimization analysis on joints between cutoff wall and connection plates of CFRD on ultra-deep overburden layer. *J. Southeast Univ. (Nat. Sci. Ed.)* **54**, 1089–1096 (2024).
7. Lin, H. et al. Research on stress and deformation characteristics and measures of anti-seepage structure of asphalt concrete core dam on ultra-deep overburden. *Water Resourc. Power.* **42**, 175–178 (2024).
8. Yu, X. et al. Study on seismic wave propagation regularity and dam-foundation interaction characteristics of earth-rock dam on deep overburden. *Comput. Geotech.* **164**, 105803 (2023).
9. Wang, F. et al. Dynamic responses of a bituminous concrete core rockfill dam on layered overburden under seismic wave input. *Comput. Geotech.* **166**, 106017 (2024).
10. Wang, Z. et al. Random dynamic response analysis of an asphalt concrete core wall dam on deep overburden with double random factors. *Comput. Geotech.* **171**, 106364 (2024).

11. Song, Z. et al. Seismic response of asphalt concrete core dam considering spatial variability of overburden foundation materials. *Arab. J. Sci. Eng.* **47**, 12605–12620 (2022).
12. Long, W. et al. Transmitting characteristics of seismic motion in super-deep overburden layer ground. *Shock. Vib.* **23**, 8898012 (2021).
13. Zhang, W. Multifield coupling numerical simulation of the seepage and stability of embankment dams on deep overburden layers. *Arab. J. Sci. Eng.* **47**, 7293–7308 (2022).
14. Zhou, Y. et al. Observations and analyses of site amplification effects of deep liquefiable soil deposits by geotechnical downhole array. *Chin. J. Geotech. Eng.* **39**, 1282–1291 (2017).
15. Li, Z. et al. Study on the effect of liquefiable overburden foundations of rockfill dams based on a pore pressure model. *Water* **18**, 2649 (2024).
16. Tang, C. et al. Investigation of the effective numerical model for seismic response analysis of concrete-faced rockfill dam on deep overburden. *Water* **22**, 3257 (2024).
17. Zhang, X. et al. Dynamic centrifuge modeling research on the propagation law of earthquake motion. *J. China Inst. Water Resourc. Hydropower Res.* **15**, 272–277 (2017).
18. Peng, W. et al. Liquefaction of deep buried sand layer based on centrifugal vibration test. *J. Changjiang River Sci. Res. Inst.* **41**, 133–138 (2024).
19. Cai, Z. et al. Liquefaction of deep overburden layers in zones with high earthquake intensity. *Chin. J. Geotech. Eng.* **42**, 405–412 (2020).
20. Peng, W. et al. Dynamic centrifugal model tests on earth rock dam resting on soft overburden. *Rock Soil Mech.* **44**, 1771–1778 (2023).
21. Yang, C. et al. Shaking table test on damage mechanism of bedrock and overburden layer slope based on the time–frequency analysis method. *Sci. Rep.* **14**, 12504 (2024).
22. Tong, X. et al. Damage evolution mechanism of rock-soil mass of bedrock and overburden layer slopes based on shaking table test. *J. Mt. Sci.* **19**, 12 (2022).
23. Tong, X. et al. Shaking table test on dynamic damage characteristics of bedrock and overburden layer slopes. *J. Test. Eval.* **2023**(51), 989–1009 (2023).
24. Lian, J. et al. Dynamic responses and evolution characteristics of bedrock and overburden layer slope with space anchor cable anti-slide piles based on large-scale shaking table test. *Soil Dyn. Earthq. Eng.* **175**, 108245 (2023).
25. Gao, Y. et al. Seismic performance of small and medium-sized homogeneous earthen dams considering valley site effects in large-scale shaking table tests. *Eng. Geol.* **318**, 107098 (2023).
26. Liu, Q. et al. Dynamic triaxial tests on seismic residual deformation characteristics of the fine-grained soil in super-deep overburden layer. *China Earthq. Eng. J.* **37**, 21–26 (2015).
27. Yang, Z. et al. Triaxial tests on dynamic deformation and strength characteristics of fine-grained soil in super-deep overburden layer. *China Earthq. Eng. J.* **36**, 824–831 (2014).
28. Kong, X. et al. Shaking table model tests on face-slab dislocation of concrete faced rock-fill dams under earthquakes. *Chin. J. Geotech. Eng.* **34**, 258–267 (2012).
29. Liu, J. et al. Large-scale shaking table model tests on seismically induced failure of concrete-faced rockfill dams. *Soil Dyn. Earthq. Eng.* **82**, 11–23 (2016).
30. Yu, T. et al. Study of dynamic characteristics of dam foundation on deep riverbed overburden with soft soil layer. *Rock Soil Mech.* **41**, 267–277 (2020).
31. Dobry, R. et al. Simplified procedures for estimating the fundamental period of a soil profile. *Bull. Seismol. Soc. Am.* **66**, 1293–1321 (1976).
32. Asgari, A. et al. Wind turbine performance under multi-hazard loads: Wave, wind, and earthquake effects on liquefiable soil. *Results Eng.* **26**, 104647 (2025).
33. Asgari, A. et al. Earthquake response analysis of soil layers using HFTD approach. *Soil Dyn. Earthq. Eng.* **26**, 320–325 (2012).
34. Ko, Y. et al. Influences of repeated liquefaction and pulse-like ground motion on the seismic response of liquefiable ground observed in shaking table tests. *Eng. Geol.* **291**, 106234 (2021).
35. Asgari, A. et al. Advanced seismic analysis of soil-foundation-structure interaction for shallow and pile foundations in saturated and dry deposits: Insights from 3D parallel finite element modeling. *Structures.* **69**, 107503 (2024).
36. Asgari, A. et al. Seismic resilience of pile groups to lateral spreading in liquefiable soils: 3D parallel finite element modeling. *Structures.* **74**, 108578 (2025).
37. Cheng, X. et al. Research progress and prospects of seismic performance on underground structure embedded in soft soil foundation. *Sci. Rep.* **14**, 21883 (2024).

Author contributions

In this study, Xing, Li and Wu are mainly responsible for the comprehensive study of technical route and shaking table model test scheme, Chen is mainly responsible for literature research and test result analysis, Ding is mainly responsible for field test work.

Funding

Declarations

Competing interests

The authors declare no competing interests.

Additional information

Correspondence and requests for materials should be addressed to L.W.

Reprints and permissions information is available at www.nature.com/reprints.

Publisher's note Springer Nature remains neutral with regard to jurisdictional claims in published maps and institutional affiliations.